Inhibition of parametric decay in heating microwave beams during fluctuations of the density profile in the edge island of Wendelstein 7-X

A. Tancetti[1], S.K. Nielsen[1], J. Rasmussen[1], D. Moseev[2], T. Stange[2], S. Marsen[2], M. Vecséi[3], C. Killer[2], G.A. Wurden[4], T. Jensen[1], M. Stejner[1], G. Anda[3], D. Dunai[3], S. Zoletnik[3], K. Rahbarnia[2], C. Brandt[2], H. Thomsen[2], M. Hirsch[2], U. Hoefel[2], N. Chaudhary[2], V. Winters[2], P. Kornejew[2], J. Harris[5], H.P. Laqua[2] and the W7-X Team*

[1] Department of Physics, Technical University of Denmark, Fysikvej, DK-2800 Kgs.Lyngby, Denmark
[2] Max Planck Institute für Plasmaphysik, Greifswald, Germany
[3] Centre for Energy Research, Budapest, Hungary
[4] Los Alamos National Laboratory, Los Alamos, NM 87545 USA
[5] Oak Ridge National Laboratory, Oak Ridge, TN 37830 USA

E-mail: tancettix@gmail.com

Abstract. Experimental evidence of parametric decay instability (PDI) is observed in the Wendelstein 7-X (W7-X) stellarator, when high-power microwave beams cross a stationary magnetic island in the plasma edge. Here, trapping and build-up of upper hybrid waves (UHWs) within a density bump (measured within the island by alkali beam emission spectroscopy, ABES) is responsible for the reduction of the instability power threshold below the maximum gyrotron power. In this paper, we provide the first experimental evidence of the connection between the trapping mechanism in the island density bump and excitation of PDI-related signals. We show correlation of periodic crashes in the PDI-related signals with quasi-continuous fluctuations in the plasma edge, which, additionally, cause a flattening of the density profile in the island. We demonstrate that flattening of the experimental density profiles can suppress the trapping mechanism and inhibit the low-threshold PDI. PDI in the edge island could alter the power deposition profile and reduce the efficiency of the electron cyclotron resonance heating system, simultaneously posing a serious threat to the optimal operation of microwave-based diagnostics and plasma-facing components.

Keywords: Parametric decay instability, electron cyclotron resonance heating, Wendelstein 7-X stellarator, upper hybrid resonance, alkali beam emission spectroscopy, island localized modes

* For the full list of the W7-X Team members, see the author list of T.S. Pedersen *et al* 2022 Nucl. Fusion 62 042022

1. Introduction

Three-wave resonant interactions are nonlinear processes taking place in media with a quadratic nonlinearity such as fluids [1, 2, 3], graphene [4], optical crystals [5, 6], opto-mechanical systems [7, 8], spatially-confined rigid membranes [9], and plasmas [10, 11, 12]. Such interactions can be parametrically driven by an intense "pump" wave, which decays into a pair of "daughter" waves if the pump power density exceeds a given threshold [13]. Similarly, the nonlinear combination of two waves can excite a third, high frequency mode.

In inhomogeneous plasmas, PDI is generally a convective instability, where daughter waves leave the decay region [14, 15, 16, 17]. However, trapping of daughter waves between adjacent reflection layers is possible in regions with a non-monotonic inhomogeneity [18, 19, 20, 21]. Here, trapped daughter waves undergo an exponential amplification in time (absolute instability), thus strengthening the nonlinear coupling with the incoming pump, and drastically decreasing the instability power threshold.

PDI in magnetized plasmas is commonly observed in astrophysics [22, 23] and extensively investigated in laboratory setups. In particular, trapping of daughter waves in non-monotonic density profiles is proposed as a key mechanism for stimulated electromagnetic emission from ionospheric plasmas. In atmospheric heating experiments, high-power radio waves injected in the atmosphere from a ground station excite, through a cascade of interactions, a population of upper hybrid waves (UHWs) trapped in density depletion regions called striations [24, 25, 26, 27]. Anomalous emission from the atmosphere observed experimentally is produced by conversion of trapped UHWs into electromagnetic waves, escaping the confinement layer.

In magnetically confined laboratory plasmas, PDI is studied in linear [28] and toroidal [29, 30] devices. In the linear machine Granite, anomalous absorption of 45 to 80 % of the microwave power injected at frequency f_0 was measured when the upper hybrid resonance (UHR) $f_{\mathrm{uh}} > f_0/2$ at symmetric layers around the maximum of the peaked density profile. Here, PDI is predicted to excite a pair of UHWs at $f_0/2$, trapped in proximity of the density maximum, between points where $f_{\mathrm{uh}} = f_0/2$.

During extra-ordinary second-harmonic (X2) electron cyclotron resonance heating (ECRH) at frequency f_0 in helical plasmas, cavities for UHWs may also be produced in magnetic islands and in filaments related to edge localized modes (ELMs). After first measurements of back-scattered microwaves around the pump frequency, f_0, during X2-ECRH in the TEXTOR tokamak [31, 32], PDI in connection with rotating magnetic islands was investigated in the ASDEX Upgrade tokamak [33]. Here, low-threshold PDI was also explored in ELM filaments [34] when the second-harmonic UHR ($f_{\mathrm{uh}} = f_0/2$) is located near the plasma edge. Experimental evidence of microwaves at $f_0/2 = 70\,\mathrm{GHz}$ with a heterodyne radiometer supports the hypothesis of PDI with excitation of two $f_0/2$ UHWs in ASDEX Upgrade. However, the decay region was never diagnosed with sufficient spatial resolution to derive precise theoretical predictions comparable with experimental results. This was possible for the first time in the Wendelstein 7-X (W7-X) stellarator [35], where the ECRH beams cross a density bump measured with high spatial resolution by alkali beam emission spectroscopy (ABES) [36] across a stationary magnetic island in the plasma edge. The theoretical model developed from ABES profiles reproduces consistently the spectrum and power of the detected PDI-related signals. However, despite the agreement between the model and the PDI-related signal, no systematic study to verify trapping has been performed yet.

PDI along ECRH microwave beams in the edge island may drain a fraction of the injected power and alter the power deposition profile. This would reduce the efficiency of the ECRH system applied in W7-X for heating, current drive, start-up, and wall conditioning [37], and motivate the inclusion of nonlinear processes in ray-tracing codes, like TRAVIS [38] for W7-X, which currently rely on a linear model for the plasma-wave interaction. Parametrically driven daughter microwaves can also damage key components of microwave-based diagnostics [39] if these are not properly shielded. Finally, electrostatic daughter modes can interact with plasma populations and generate supra-thermal ion/electron populations [40, 41], which, on the one hand, could potentially represent an auxiliary heating mechanism, while on the other hand, could degrade plasma facing probes [42, 43]. A deeper understanding of low-threshold PDI in W7-X is, thus, not only essential to validate the current theoretical models for absolute instabilities in non-monotonic density profiles, but also to optimize the efficiency of microwave-based systems, essential components on the way to a burning fusion plasma.

In this paper, we experimentally confirm that wave trapping is essential for PDI in W7-X. We present crashes in the PDI-related signal measured in W7-X and demonstrate a correlation with fluctuations in the plasma edge, related to so-called island localized modes (ILMs) [44, 45, 46, 47]. We show that in the standard magnetic configuration, with a chain of five large islands cut by the divertor plates in the plasma edge, quasi-continuous oscillations are measured by several diagnostics in the plasma edge and induce a

periodic flattening of the density profile in the island. We argue that the instability power threshold for a flat density profile exceeds substantially the injected microwave power [48, 49], resulting in absence of the PDI-related signal.

The article is organized as follows. Section 2 summarizes the theoretical mechanisms for trapping of UHWs within a non-monotonic density profile and the model for PDI in W7-X. Section 3 introduces the experimental setup and sets the stage for the experimental results described in section 4. In section 5, we study the connection between the island density profile and the PDI-related signal during quasi-continuous oscillations in the plasma edge and propose inhibition of the instability due to the flattening of the density profile. Finally, we draw our conclusions in section 6.

2. Wave trapping and model for PDI in W7-X

In magnetized plasmas, trapping of UHWs within a non-monotonic density profile can reduce the PDI power threshold below the typical maximum gyrotron power, $\sim 1\,\mathrm{MW}$. In order to describe the trapping mechanism, we consider the solid and the dashed 1D (blue) density profiles along the x-axis in figure 1.a, which both have a local density maximum at $x = 0\,\mathrm{cm}$. We assume a uniform background magnetic field along the z-axis, perpendicular to the x-axis, $\mathbf{B} = B\,\hat{z}$ with $B = 2.23\,\mathrm{T}$, and electron temperature $T_\mathrm{e} = 40\,\mathrm{eV}$, which are typical values in the edge island of W7-X. We plot the resulting dispersion curves for the cold (k^-, X-mode) and the warm (k^+, electron Bernstein wave, EBW) branches of the dispersion relation for UHWs at $\tilde{f} = 65\,\mathrm{GHz}$ [50]

$$k^{\pm} = \sqrt{-\frac{S}{2\ell_{\mathrm{T_e}}^2}\left(1 \pm \sqrt{1 + \frac{16\pi^2\tilde{f}^2\ell_{\mathrm{T_e}}^2}{c^2}\frac{S^2 - D^2}{S^2}}\right)}, \quad (1)$$

where c is the speed of light in vacuum,

$$S = 1 - \frac{f_{\mathrm{pe}}^2}{\tilde{f}^2 - f_{\mathrm{ce}}^2},\ D = \frac{f_{\mathrm{ce}}}{\tilde{f}}\frac{f_{\mathrm{pe}}^2}{\tilde{f}^2 - f_{\mathrm{ce}}^2}, \quad (2)$$

are the components of the cold dielectric tensor at $\tilde{f}$ as introduced by Stix [51], and

$$\ell_{\mathrm{T_e}} = \rho_\mathrm{e}\sqrt{\frac{3f_{\mathrm{pe}}^2 f_{\mathrm{ce}}^2}{(4f_{\mathrm{ce}}^2 - \tilde{f}^2)(\tilde{f}^2 - f_{\mathrm{ce}}^2)}}, \quad (3)$$

is the thermal length.

The electron plasma and cyclotron frequency are $f_{\mathrm{pe}} = (q^2 n_\mathrm{e}/(4\pi^2 m_\mathrm{e}\varepsilon_0))^{1/2}$ and $|f_{\mathrm{ce}}| = qB/(2\pi m_\mathrm{e})$, respectively, where q is the elementary charge, m_e is the electron mass, and ε_0 is the vacuum permittivity. Lastly, $\rho_\mathrm{e} = (T_\mathrm{e} m_\mathrm{e})^{1/2}/(qB)$ is the electron Larmor radius. The solid dispersion curves in figure 1.a are produced by the solid density profile, while evanescent regions, where the density is too low to allow propagation of UHWs, are pink-shaded. The closed loop in $k(x)$ around the local density maximum implies trapping of UHWs, with mode conversion at the turning points, where $f_{\mathrm{uh}} = \tilde{f}$. In a stationary state, for a mode confined within the density bump, the total phase shift along a single transit must equal a multiple of 2π plus a $-\pi/2$ factor for each reflection [52]. This constraint, known as the Bohr−Sommerfeld

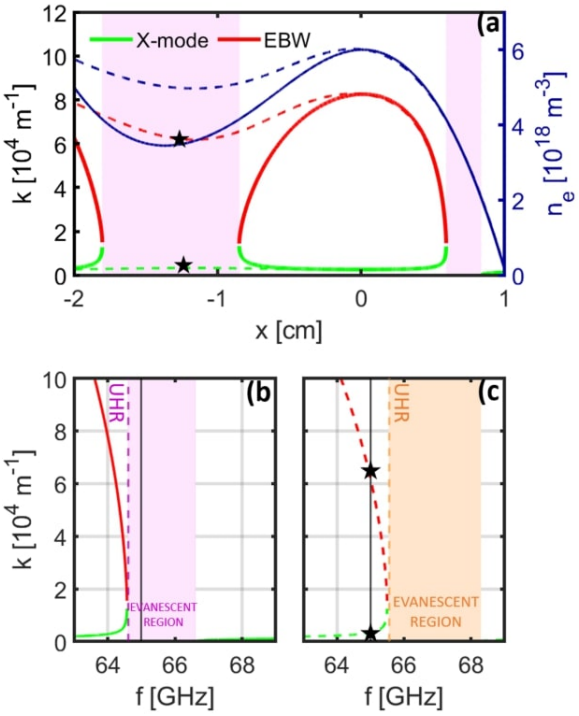

Figure 1: a) Density profiles (blue) and resulting dispersion curves for the warm (red) and the cold (green) branches of the UHW dispersion relation at $\tilde{f} = 65\,\mathrm{GHz}$, for $B = 2.23\,\mathrm{T}$ and $T_\mathrm{e} = 40\,\mathrm{eV}$ (these values are also assumed in panels b) and c)). Solid (dashed) dispersion curves correspond to the solid (dashed) density profile, whereas pink-shaded areas highlight evanescent regions for the solid density profile. b) Dispersion relation for UHWs around the UHR for $n_{\mathrm{e},1} \approx 3.5 \times 10^{18}\,\mathrm{m}^{-3}$ and c) $n_{\mathrm{e},2} \approx 5 \times 10^{18}\,\mathrm{m}^{-3}$, values of the local density minimum for the solid and the dashed density profile in a), respectively. The evanescent region is pink-shaded in b) to illustrate the connection with the top panel whereas it is orange-shaded in c). In b) and c), the vertical line shows frequency $\tilde{f} = 65\,\mathrm{GHz}$. In the latter case, the two modes at $\tilde{f}$, identified by black stars (same in a), can propagate all the way to the left of the local density maximum.

quantization condition, reads

$$\int_{x_l}^{x_r} |k^+| - |k^-|\, dx = (2\alpha + 1)\pi, \tag{4}$$

where x_l and x_r are the coordinates of the turning points, and $\alpha \in \mathbb{N}$ is the eigenvalue of the trapped mode.

Mode conversion is further clarified in figure 1.b, where the dispersion relation in eq. (1) is shown for $B = 2.23\,\mathrm{T}$, $T_\mathrm{e} = 40\,\mathrm{eV}$, and $n_{\mathrm{e},1} \approx 3.5 \times 10^{18}\,\mathrm{m}^{-3}$, corresponding to the local minimum of the solid density profile. Here, it is possible to see that the cold (green) and the warm (red) branches of the dispersion relation represent waves propagating in opposite directions (with opposite sign of the group velocity $\mathbf{v}_\mathrm{g} = \mathrm{d}\omega/\mathrm{d}k$, where $\omega = 2\pi f$ is the angular frequency of the wave), and describe mode conversion in proximity of the UHR (merging point). The pink-shaded evanescent region lies between the UHR, $f_\mathrm{uh} = f_\mathrm{ce}(1+\eta)^{1/2}$, on the left, and the R-cutoff, $f_\mathrm{R} = f_\mathrm{ce}[1 + (1+4\eta)^{1/2}]/2$, with $\eta = (f_\mathrm{pe}/f_\mathrm{ce})^2 \propto n_\mathrm{e}$, and therefore extends across different frequency ranges for different values of n_e. For $n_\mathrm{e} = n_{\mathrm{e},1}$, $\tilde{f}$ (vertical black line) falls within the evanescent region, confirming the possibility of localization of UHWs at $\tilde{f}$ below the local maximum of the solid density profile. Conversely, for $n_\mathrm{e} = n_{\mathrm{e},2} \approx 5 \times 10^{18}\,\mathrm{m}^{-3}$, the local minimum of the dashed density profile, (see the plot of $k(f)$ in figure 1.c) $\tilde{f}$ lies outside the evanescent region and intersects both branches of the dispersion relation as shown by the black stars in figure 1.c. In this case, the value of the local density minimum remains high enough to allow propagation of UHWs, thus precluding localization of waves around the local maximum. Consistent with this, the dashed dispersion curves in figure 1.a, corresponding to the dashed density profile, stretch without interruptions to the left of the local density maximum.

In scenarios with (approximately) constant magnetic field, a non-monotonic density profile, such as the solid curve in figure 1.a, is responsible for localization of UHWs in a spatial region between UH layers. Fluctuations of the local density minimum can, however, suppress the trapping mechanism and prevent local amplification of thermal UHWs.

In the final part of this section, we provide a brief summary of the theoretical model of PDI in W7-X, and refer to [35] for further details. Suppose an X-mode pump wave with frequency f_0 and wavenumber k_0 is injected from the right-hand side of figure 1.a and crosses the solid density profile. Amplification of UHWs above the thermal level in the trapping region strengthens the nonlinear coupling with the incoming pump wave, and hence allows PDI with a power threshold of a few hundred kW. The pump wave can then decay into an UH mode $(f_1, k_1^\pm)$, with $f_1 < f_0/2$, and $k_1^\pm$ given in eq. (1), and an escaping fast X-mode, with (f_2, k_2), if the resonance conditions $f_0 = f_1 + f_2$ and $k_0 = k_1 + k_2$ are satisfied in the trapping region. Build-up of primary UHWs in the trapping layer saturates through secondary decay into a pair of trapped waves: a slightly down-shifted UHW, f_3, and a low frequency ion Bernstein wave (IBW), with $f_4 = 0.93\,\mathrm{GHz}$. Higher order plasma instabilities excite high-frequency waves with $f_5 = f_0 - f_4$ and $f_6 = f_0 + f_4$, i.e. down- and up-shifted from the pump frequency, respectively. The model predicts a power threshold of $P_\mathrm{thr} \approx 300\,\mathrm{kW}$, in agreement with the experimental power threshold, $P_\mathrm{xp} \approx 320\,\mathrm{kW}$, and a fraction of power drained from the pump by PDI in the experiment in [35] of approximately 4 %.

The model was developed for shot 20180821.012, one of the few discharges with measurements of PDI-related activity and simultaneous ABES profiles. Even though the PDI-relevant discharge to be discussed here, 20180821.024, is very similar (in terms of magnetic configuration, microwave power, and line integrated density) to the reference program of [35], lack of ABES data prevents precise predictions for this specific case. However, based on the fact that ABES generally detects a non-monotonic density profile across the broad equatorial plane magnetic island of the standard configuration, on the similarity between the two discharges, and between the spectra of the PDI-related sidebands, we can assume a similar PDI cascade in the discharge presented here.

3. Experimental setup

Wendelstein 7-X

Here, we describe experiments performed in the W7-X stellarator [53, 54] during the third experimental campaign, OP1.2(b)[55]. A set of 50 non-planar and 20 planar superconducting coils produces the nested magnetic flux surfaces and chains of stationary magnetic islands at rational values of the rotational transform [56]. In the standard magnetic configuration, a chain of five magnetic islands is created in the plasma edge, as shown in the Poincaré plot in figure 2.a. The device relies on the island divertor concept [57] for particle and heat exhaust which exploits the island chain in the plasma edge in order to focus the heat load on the divertor targets.

In magnetic configurations with an inner island chain (at $\sim 70 - 90\,\%$ of the minor radius), where islands do not cut the divertor plates, ILMs [45] are observed by several diagnostics in the island regions. Each ILM event may induce a flattening and an increase of $\sim 20\%$ of the density profile around the last closed flux surface [58]. As the island chain is shifted closer to the divertor plates, ILMs evolve into quasi-continuous os-

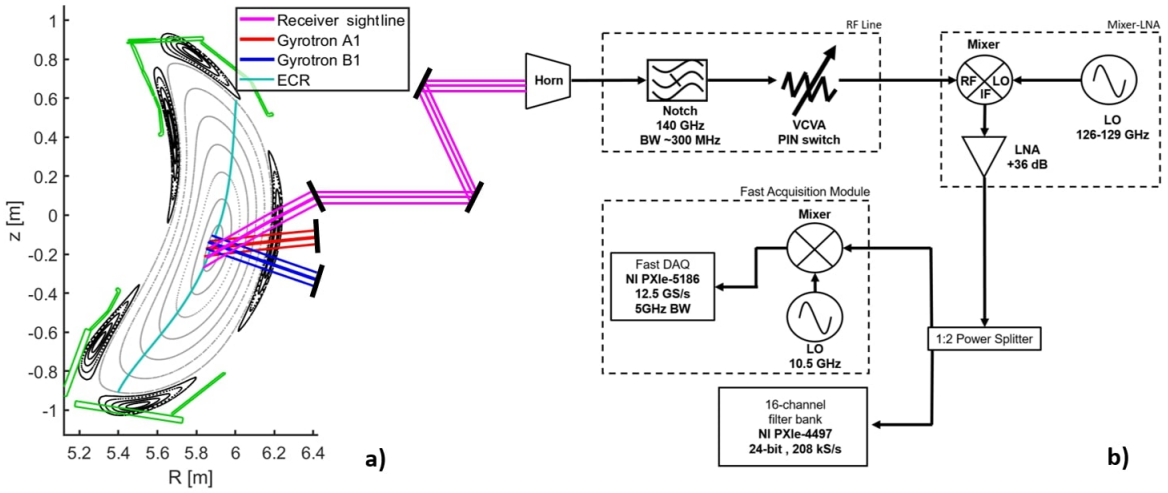

Figure 2: a) Poincaré plot of the standard magnetic configuration for the two discharges discussed in the paper at toroidal angle $\phi = 354°$. Grey and black curves represent the plasma confinement region and the five magnetic islands, respectively, while green plates are the poloidal cross-section of the divertor targets, cut by the stationary islands. Two microwave beams, from gyrotron A1 (red) and B1 (blue) are injected from the right-hand side and heat the plasma at the ECR (cyan), while the magenta beam shows the CTS line-of-sight in shot 20180821.024, termed PDI-relevant discharge. b) Block diagram of the CTS receiver in W7-X.

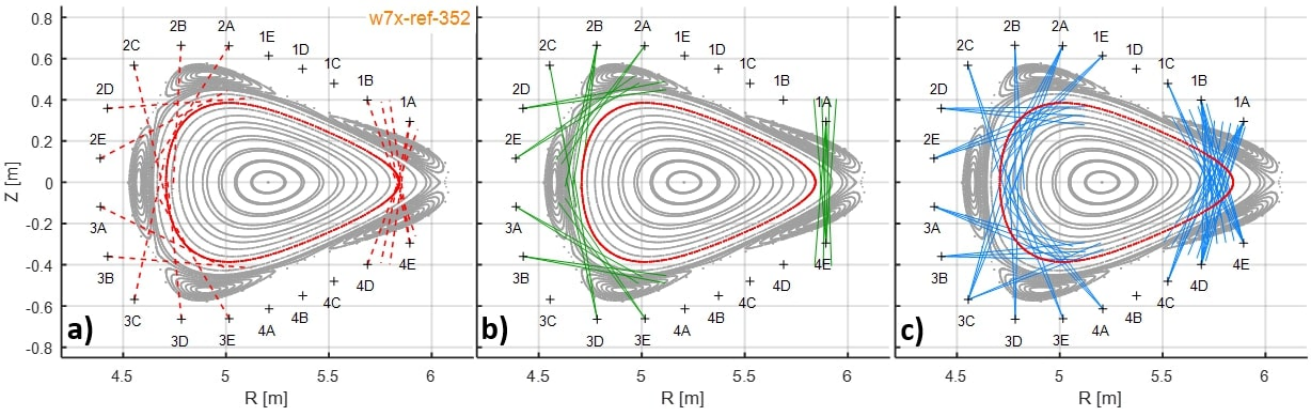

Figure 3: Layout of the cameras of the XMCTS (crosses) at $\phi = 36°$ and corresponding Poincaré plot of the standard magnetic configuration for the PDI-relevant discharge (20180821.024). a) Red dashed lines show inversion chords, tangent to the inversion surface which is outlined with a solid red curve. b) Green and c) blue chords are tangent to magnetic surfaces outside and inside the inversion surface, respectively, and are, thus, termed "outward"and "inward" chords.

cillations with frequency ranging from a few hundred Hz up to a few kHz [45].

In the experiments discussed here, the hydrogen plasma is sustained by X2-ECRH with two 1-MW gyrotrons (A1 and B1) at frequency $f_0 = 140\,\mathrm{GHz}$ [37]. The microwave beams are injected from the steerable mirrors on the right-hand side of figure 2.a, cross the centre (O-point) of the equatorial-plane magnetic island, and reach the ECR in the plasma core.

Collective Thomson scattering

Signals related to PDI are monitored with a heterodyne radiometer with a steerable line-of-sight (magenta in figure 2.a) developed for collective Thomson scattering (CTS) [59]. In the following, we describe the details of the radiometer setup.

As shown in figure 2.b, the main components of the receiver can be grouped into three blocks: a radio-frequency (RF) line, a Mixer-LNA (Low-Noise-Amplifier) block, and a dual back-end acquisition system. The radiation from the transmission line

enters the RF line via a horn antenna and it is led through a cascade of two notch filters and a Voltage Controlled Variable Attenuator, VCVA, in order to protect the electronics from the gyrotron stray radiation. In the mixing stage, a frequency mixer, in combination with a local oscillator (LO) arrangeable between 126 and 129 GHz, shifts the input signal from the waveguide F-band ($90-140$ GHz) to the X-band ($8-12$ GHz), and sends the signal to a LNA before the IF processing stage.

The CTS receiver is equipped with a dual back-end: 16-channel filter bank with a frequency range $5-17$ GHz and a fast acquisition module. Since only the latter is relevant for the present discussion, we refer the reader to [60] for technical details on filter banks.

In the fast acquisition module, a second mixing stage allows a further down-shift of the CTS signal, finally sent to the National Instrument PXIe-5186 analog-to-digital converter (ADC). The ADC has a maximum sampling rate of $f_{\rm s}^{\rm max} = 12.5$ GSamples/s (but usually operated at $f_{\rm s} = 6.25$ GSamples/s), a bandwidth of 5 GHz, and on-board memory of 1 GB [59, 60]. With an 8-bit dynamic range, for each discharge 160 ms of acquisition time can be stored in the memory (at $f_{\rm s} = 6.25$ GSamples/s). However, a first-in first-out algorithm allows the acquisition time to be extended significantly. For PDI-relevant shots, the CTS acquisition trigger generally has a standard duty cycle of $d_{\rm off}^{\rm on} = \tau_{\rm on}/(\tau_{\rm on}+\tau_{\rm off}) = 8.3\,\%$, with $\tau_{\rm on} = 0.5$ ms and $\tau_{\rm off} = 5.5$ ms.

Spectral information (in $\rm V^2/Hz$) is extracted with the MATLAB fast Fourier transform algorithm, using a window length $n_{\rm FFT} = 2^{12} = 4096$, and Hann window function. The resulting frequency and time resolutions are $\delta f = f_{\rm s}/n_{\rm FFT} = 1.53$ MHz and $\delta t = 0.6\,\mu s$, respectively. Finally, the signal is calibrated using the emission spectra of two blackbody sources at room temperature and at liquid nitrogen temperature. Details of the calibration are given in [60].

Auxiliary diagnostics

A set of auxiliary diagnostic systems is employed to monitor the density and the evolution of quasi-continuous oscillations in the plasma edge.

Radial profiles of the electron density across the equatorial-plane magnetic island, $n_{\rm e}$, are provided by the ABES with high spatial, $\delta r_{\rm n} \sim 5$ mm, and time resolution $\delta t_{\rm n} \sim \mu$s [36].

For the study of edge fluctuations, the systems employed in this work are an X-ray multi-channel tomography system (XMCTS) [61], a continuous Rogowski coil [62] for measurements of the plasma current, $I_{\rm p}$, ECE [63], and filterscopes for Hα radiation [64].

In the XMCTS, a set of 20 cameras with 18 lines-of-sight each is arranged around a triangular cross-section at toroidal angle $\phi = 36°$, and measures line-integrated soft X-rays ($1-12$ keV) radiation. The camera layout is shown with crosses in figure 3.a, all around the Poincaré plot of the standard magnetic configuration. In the study of ILMs and quasi-continuous oscillations, XMCTS plays a key role to localize the mode radially and poloidally with high time resolution, $\delta t_{\rm X} = 0.5\,\mu$s. The ECE system in W7-X makes use of a heterodyne radiometer to measure T_e at 32 radial positions, along a line-of-sight with monotonically increasing magnetic field, at 2 MHz acquisition rate. The detected frequency ranges from $f_{\rm l} = 126.4$ GHz, on the low field side (LFS) to $f_{\rm h} = 161.6$ GHz, on the high field side (HFS). Time-traces of $T_{\rm e}$, when correlated with the patterns detected by XMCTS chords, are useful to infer the radial position of ILMs and quasi-continuous fluctuations [65]. Finally, Hα filterscopes measure the red spectral line of the Balmer series at wavelength $\lambda_{\rm H\alpha} = 656.28$ nm. Since the corresponding energy gap is $E_{\rm H\alpha} \approx 1.9$ eV, the emission predominantly takes place in the plasma edge.

4. Experimental results

Ideally, we would focus on a single discharge where observations of PDI-related signals can be directly correlated with high time resolution ABES profiles. Unfortunately, such a shot is not available among the experiments carried out so far in W7-X. One of the few discharges where PDI can be investigated from ABES density profiles is discussed in [35]. However, in that case the ABES acquisition rate is below 10 Hz, and thus is not suitable for the study of edge fluctuations. For this reason, we have instead identified two discharges and compared crashes in the PDI-related signals in a so-called PDI-relevant discharge (20180821.024, without ABES measurements) with ABES density fluctuations in the plasma edge, in discharge 20180906.017, termed ABES-relevant (without CTS measurements). The experiments of interest were selected as similar as possible in terms of time-traces of the total microwave power and line integrated density for the time interval of interest (shown in figure 4), and magnetic configuration. They were both performed in the standard magnetic configuration with on-axis magnetic field $B_{0,\rm pdi} = 2.52$ T in the former, and $B_{0,\rm abes} = 2.62$ T in the latter. For discharges with a plasma beta close to one, $\beta \approx 1\%$, like the latter case, the theoretical on-axis magnetic field is increased to compensate the outward radial shift of the plasma column (Shafranov and the diamagnetic shifts). This allows to keep the EC resonance ($B_0 = 2.52$ T) on the

actual magnetic axis.
The red thread between the selected experiments is the presence of similar quasi-continuous fluctuations in the plasma edge of the standard configuration.

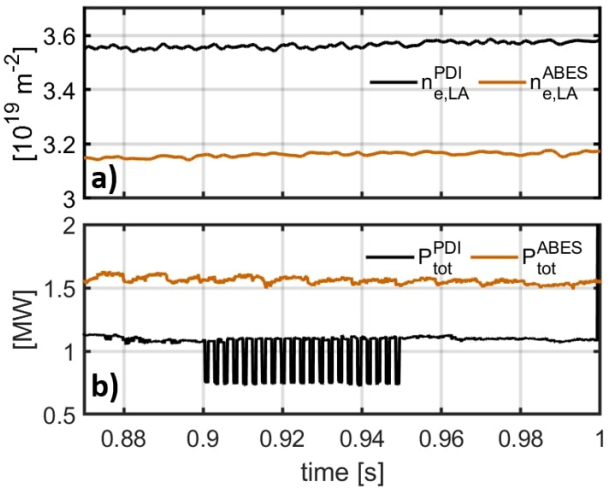

Figure 4: Time-traces of a) the line integrated density, $n_{\mathrm{e,LA}}$, and b) the total microwave power, P_{tot}, for the time interval of interest in the PDI- and the ABES-relevant discharges.

A comparison between the line integrated density, $n_{\mathrm{e,LA}}$, and the total microwave power, P_{tot}, in the two discharges is shown in figure 4.a and 4.b, respectively, for the time interval under consideration in the following discussion. Different colors are used for the PDI- and the ABES-relevant shots. In both discharges, P_{tot} and $n_{\mathrm{e,LA}}$ remain approximately constant, with a gap between discharges of $\Delta P_{\mathrm{tot}} = |P_{\mathrm{tot}}^{\mathrm{ABES}} - P_{\mathrm{tot}}^{\mathrm{PDI}}| \approx 0.5\,\mathrm{MW}$ and $\Delta n_{\mathrm{e,LA}} = |n_{\mathrm{e,LA}}^{\mathrm{ABES}} - n_{\mathrm{e,LA}}^{\mathrm{PDI}}| \approx 0.4 \times 10^{19}\,\mathrm{m}^{-2}$. A fast modulation of the power from gyrotron A1 is performed in the PDI-relevant shot with frequency $f_{\mathrm{mod,A1}} \approx 420\,\mathrm{Hz}$ ($1/f_{\mathrm{mod,A1}} \approx 2.4\,\mathrm{ms}$) between $t = 0.9 - 0.95\,\mathrm{s}$.
Time-traces of the microwave power injected with the heating gyrotrons during the start-up phase ($t = 0 - 1\,\mathrm{s}$) of the PDI-relevant discharge are plotted in figure 5.a. While B1 is slowly modulated between $P_{\mathrm{B1}} = 250$ and $500\,\mathrm{kW}$, the power from gyrotron A1 remains at $P_{\mathrm{A1}} \approx 800\,\mathrm{kW}$, with the exception of the fast modulation between $t = 0.9 - 0.95\,\mathrm{s}$, where P_{A1} reaches a minimum of $550\,\mathrm{kW}$. Figure 5.a also shows the time-trace of the line integrated density (dashed curve), increasing slowly from $n_{\mathrm{e,LA}} \approx 0.18$ to $0.35 \times 10^{20}\,\mathrm{m}^{-2}$.
The resulting CTS mean spectrogram is plotted in figure 5.b, with frequency shift from the reference gyrotron A1 in GHz, Δf_{A1}, on the y-axis. Around $\Delta f_{\mathrm{A1}} = 0\,\mathrm{GHz}$, the notch filter frequency range is outlined with white solid lines and encloses the thin yellow lines produced by the stray radiation of the start-up gyrotrons. It is worth noting here that the slow power modulation of B1 produces a chirping of the gyrotron frequency with respect to the reference source A1. Up- (U-SB) and down-shifted (D-SB) sidebands are the PDI-related signals (corresponding to the signals at f_6 and f_5 in the theoretical model) stretching symmetrically around $\Delta f_{\mathrm{A1}} = 0\,\mathrm{GHz}$ from $t \approx 0.2$ until $1\,\mathrm{s}$. The U-SB evolves without major interruptions from harmonics around $\Delta f_{\mathrm{A1}} \approx 0.8\,\mathrm{GHz}$, at $t \approx 0.2\,\mathrm{s}$, up to harmonics at $\Delta f_{\mathrm{A1}} \approx 1.1\,\mathrm{GHz}$, whereas the D-SB displays a number of different components. Among these, one component displays the chirping of the gyrotron B1 and could thus be excited by this gyrotron (as pointed out in figure 5.b). During the interval $t = 0.9 - 1\,\mathrm{s}$, the CTS acquisition duty cycle was increased from the standard $d = 8.3\,\%$ to $d = 83\,\%$ (with $\tau_{\mathrm{off}} = 0.1\,\mathrm{ms}$) in order to monitor the evolution of the PDI side-bands with higher resolution during the fast modulation of P_{A1}, interrupted at $t = 0.95\,\mathrm{s}$ (see figure 5.c). The PDI-related side-bands in the time interval from $t = 0.93 - 1\,\mathrm{s}$ are shown in panels 5.d and 5.e. Each side-band contains a pair of harmonics, shifted from each other by approximately 35 MHz (comparable to the ion cyclotron frequency for $B = 2.23$ T, $f_{ic} = 34$ MHz), and parallel to the signal produced by gyrotron A1. For $t < 0.95\,\mathrm{s}$, both PDI side-bands are significantly damped when $P_{\mathrm{A1}} \approx 550\,\mathrm{kW}$, whereas after $t = 0.95\,\mathrm{s}$ simultaneous crashes in the PDI side-bands are visible with frequency $f_{\mathrm{gray}} \approx 120\,\mathrm{Hz}$, despite absence of power modulation.
Computing the integral of the SPD in figures 5.d-e within the shown frequency ranges and plotting the resulting (normalized) power during the interval $t = 0.95 - 0.995\,\mathrm{s}$, yields the time-traces in figure 6.a for the up-, s_{u}, and the down-shifted band, s_{d}. Here, gray-shaded regions highlight crashes in the PDI side-bands where $s_{\mathrm{u}}^{\mathrm{max}} - s_{\mathrm{u}}^{\mathrm{min}} > 0.5$, and $s_{\mathrm{u}}^{\mathrm{max/min}}$ are the values of s_{u} at a given local maximum and at the following minimum, respectively. The duration of the crashes is in the order of $\tau_{\mathrm{gray}} \sim 1 - 2\,\mathrm{ms}$. Simultaneous fluctuations in the plasma edge are detected by multiple diagnostics. Time-traces of soft X-rays measured along different chords are shown (blue) in figure 6.b. The signals along inversion chords, red in figure 3.a, oscillate at $f_{\mathrm{inv}} \approx 300\,\mathrm{Hz}$ and are tangent to a specific magnetic surface, the inversion surface, plotted red in figure 3.a-c. Outward viewing chords (green in figure 3.b) and inward viewing chords (blue in figure 3.c) look outside and inside the inversion surface, respectively, and measure fluctuations at $f_{\mathrm{crash}} \approx f_{\mathrm{inv}}/2 = 150\,\mathrm{Hz}$, albeit phase shifted by $\varphi \approx \pi\,\mathrm{rad}$. Crashes in the PDI-related side-bands coincide with crashes in the inward and peaks in the outward viewing chords.

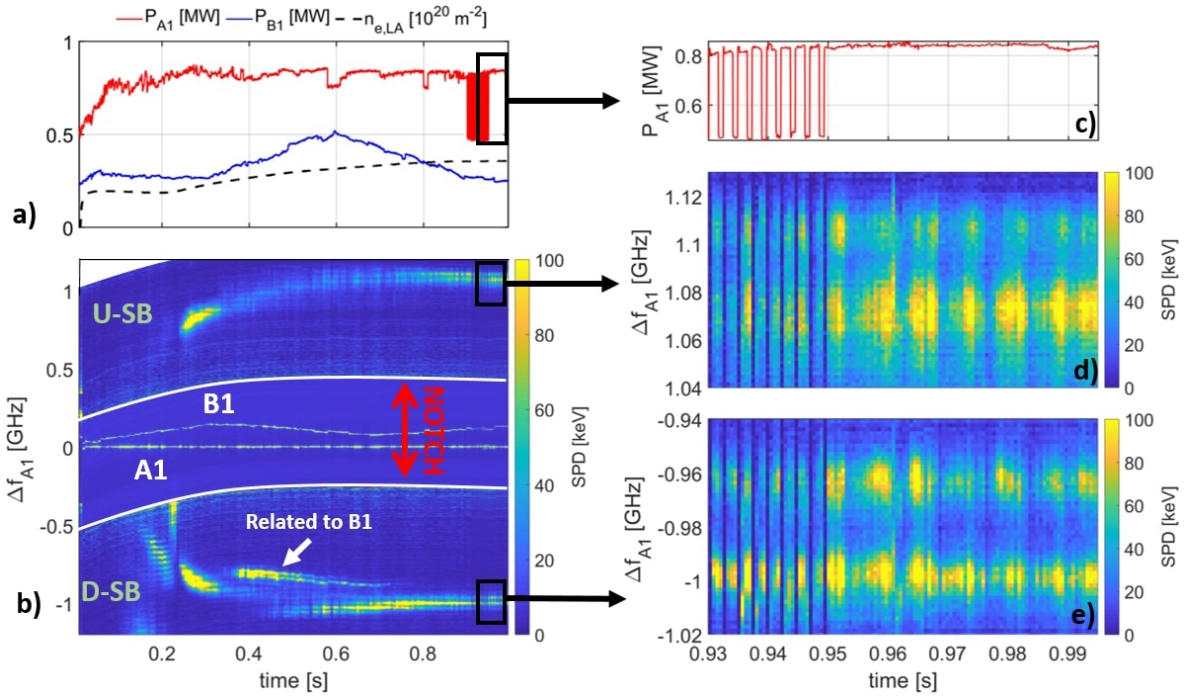

Figure 5: a) Time-traces of the gyrotron power, P_{A1} and P_{B1}, and line integrated density, $n_{\mathrm{e,LA}}$, during the start-up phase in discharge 20180821.024. b) Resulting CTS spectral power density (SPD). PDI-related side-bands appear symmetrically up- (U-SB) and down-shifted (D-SB) from the reference gyrotron frequency (A1). c) Zoom-in on P_{A1}, d) on the up-shifted, and e) on the down-shifted bands in $t = 0.93-0.995\,\mathrm{s}$ (high acquisition duty cycle). The two harmonics in each side-band, separated by $\sim 35\,\mathrm{MHz}$, are strongly damped during modulation of P_{A1}. For $t > 0.95\,\mathrm{s}$, both side-bands still display simultaneous crashes.

Time-traces of T_{e} from some ECE channels in the plasma edge show fluctuations correlated with PDI crashes and XMCTS signals. In figure 6.b, an ECE channel on the LFS is shown to oscillate in phase with the inward SXR chords whereas a channel on the HFS is correlated with the signal from the inversion chords. Finally, peaks corresponding to the crashes in the PDI-related sidebands are observed in time-traces of the Hα light and of the plasma current, I_{p}, plotted in figure 6.c. Since the ABES did not operate in the PDI-relevant discharge, we now discuss the second (ABES-relevant) discharge, 20180906.017, with high time resolution ABES profiles, $\delta t_{\mathrm{ABES}} = 20\,\mu\mathrm{s}$, but without CTS measurements.

Figures 6.d-f compare time-traces from different diagnostics for shot 20180906.017 between $t = 0.87-0.92\,\mathrm{s}$. Panel 6.d shows the time evolution of the ABES density at $R \approx 6.233\,\mathrm{m}$, where the local minimum of the density bump is usually found in the standard magnetic configuration (see figure 7.a). Gray-shaded areas identify density bursts* corresponding to flattening of the radial density profile within the island. The complete density profile before, during, and after the burst in the red-shaded region, at $t \approx 0.89\,\mathrm{s}$, is shown in figure 7.a-c. Before the event (see figure 7.a), ABES measures a non-monotonic density profile with a local maximum in proximity of the centre of the island. In agreement with [58], during the event (panel 7.b) the density at the local minimum grows by approximately 25 %, with a simultaneous growth of only 5 % at the local maximum producing the flatter density profile shown in figure 7.b. After the burst (figure 7.c), the profile returns to the initial non-monotonic profile. During density bursts (gray-shaded areas in figure 6.d), inward and outward XMCTS chords observe crashes and peaks respectively, while inversion chords reveal the standard transition pattern, with low peaks and mild crashes (figure 6.e).

A similar evolution can be seen in the ECE channels on the LFS of the plasma. While the signal of the channel in proximity of the LCFS is strongly correlated with the crashes of the inward XMCTS chords, an inner, adjacent channel (number 6) measures fluctuations similar to the inversion chords. Finally, figure 6.f reveals strong peaks in the plasma current and in the Hα light emission during the density fluctuations in the plasma edge.

* see Appendix A for details on criteria to select relevant events

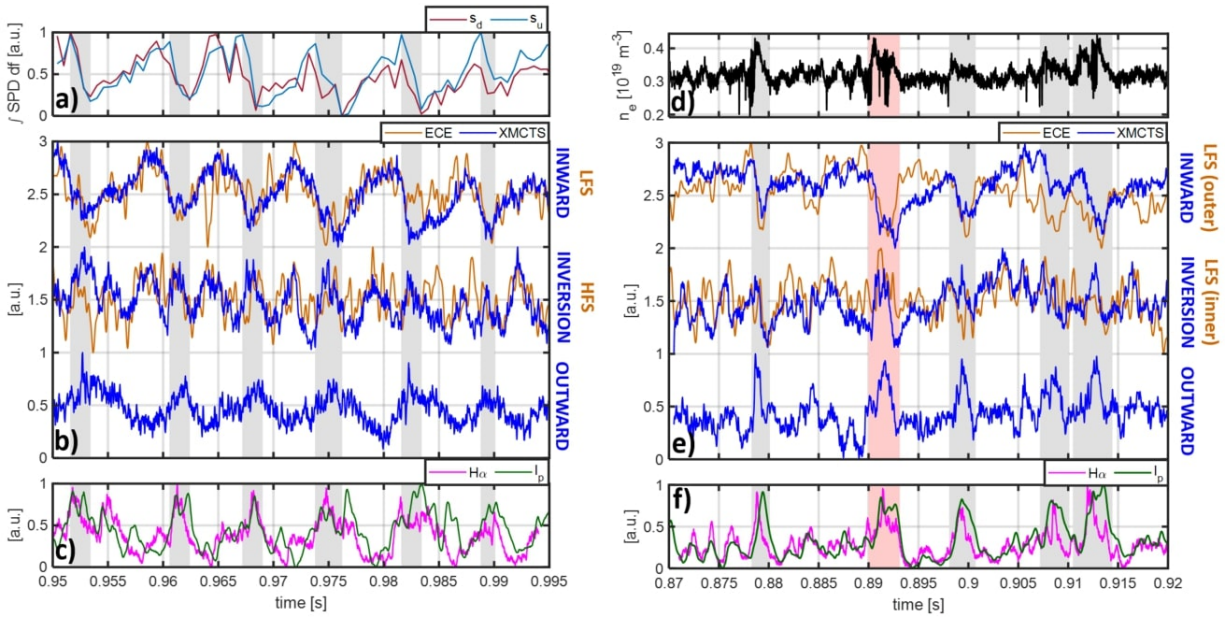

Figure 6: a-c) Time-traces from the PDI-related discharge 20180821.024 during the interval $t = 0.95 - 0.995$ s. a) Normalized integrated SPD for the up-shifted, $s_{\rm u}$, and the down-shifted side-band, $s_{\rm d}$. Gray-shaded regions identify crashes in $s_{\rm u}$ where $s_{\rm u}^{\rm max} - s_{\rm u}^{\rm min} > 0.5$. b) Normalized time-traces of soft X-rays along an inward, an inversion, and an outward chord, together with normalized $T_{\rm e}$ from two edge ECE channels (channel 2, LFS; channel 28, HFS). The signals are vertically separated by an artificial offset in order to highlight the trends more clearly. c) Time-traces of the Hα light from tube AEL30 (magenta), with a time delay of -1 ms (signal shifted to the left) and plasma current (green), $I_{\rm p}$. d-f) Time-traces from the ABES-relevant discharge, 20180906.017, during the interval $t = 0.87 - 0.92$ s. d) ABES density at $R \approx 6.233$ m (local minimum). The gray-shaded regions highlight density bursts and synchronized fluctuations in the plasma edge. The time evolution of the complete density profile for the event in the red-shaded area is shown in figure 7.a-c. e) Normalized Soft X-rays signal (blue) along an inward, an inversion, and an outward chord (all with time delay 0.5 ms, i.e. signals shifted to the right), and normalized $T_{\rm e}$ from two ECE channels (brown) in the LFS (channel 5, outer; channel 6, inner). Similarly to b), a vertical offset is applied to the signals to visualize the fluctuations more clearly. f) Time-traces of the Hα light from tube AEK41 (magenta), with time delay 1 ms, and plasma current (green), $I_{\rm p}$.

5. Discussion

In the PDI-relevant discharge, correlation of the crashes in the PDI-related side-bands (gray-shaded in figure 6.a) with oscillations in the plasma edge (Hα, XMCTS outward chords) suggests excitation of PDI in the edge. In the ABES-relevant discharge, fluctuations in the plasma edge with frequency $f_{\rm gray}$ and duration $\tau_{\rm gray}$ comparable to those measured during PDI crashes are observed by the same set of diagnostics and are accompanied by a flattening of the ABES density profile across the island (gray-shaded in figure 6.d).
The similarity between edge fluctuations in the two discharges suggests a connection with quasi-continuous oscillations generally observed in the standard magnetic configuration [45]. Furthermore, the fact that the edge plasma essentially displays the same trend during PDI crashes and ABES density bursts (e.g. peaks in the outward XMCTS), indicates a direct connection between these events. Trapping of UHWs indeed requires the formation of a density bump in the magnetic island, as shown in figure 7.a. Here, dispersion curves for slow X-mode waves (green), $k_{\rm X}$, and EBWs (red), $k_{\rm ebw}$, at $f_1 = 64.45$ GHz, are plotted for $B = 2.23$ T below the mean density profile before the event at $t \approx 0.89$ s in figure 6.d. The closed loop between pink-shaded evanescent regions suggests trapping of UHWs, and hence the possibility of a low-threshold PDI in the ECRH beam crossing the inhomogeneity. When the density profile is flattened (see figure 7.b) trapping is precluded, resulting in inhibition of the low-threshold PDI. The instability power threshold in this scenario might increase significantly above the maximum gyrotron power (1 MW), thus producing gaps in the PDI-related side-bands. After the density burst, the non-monotonic density profile and the related confinement layer for UHWs are restored (see figure 7.c) supporting the low-threshold PDI again. Flattening of the density profile measured by ABES in the standard configuration is in

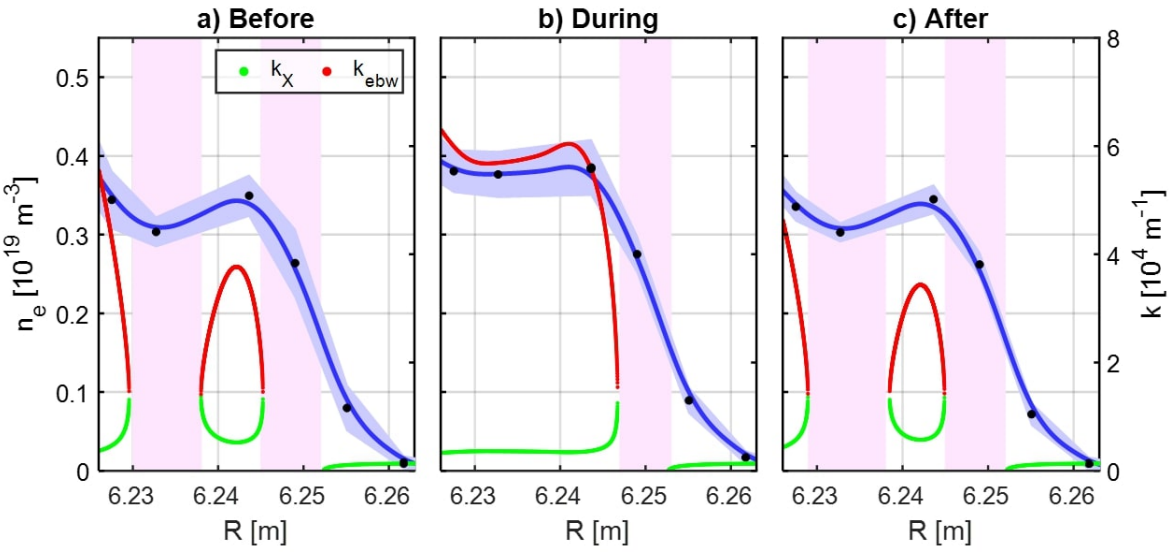

Figure 7: ABES density profiles (spatial resolution $\delta r_{\rm n} \sim 5\,$mm) within the equatorial-plane magnetic island and resulting dispersion curves for UHWs. ABES density values averaged over 50 profiles corresponding to $\tau = 1$ ms at $t \approx 0.89$ s in the ABES-relevant discharge are shown with black points while solid blue profiles are built from the same values with a slight smoothing and shaded blue regions show the standard deviation. Resulting dispersion curves for UHWs at $f_1 = 64.45$ GHz with X-mode waves in green, $k_{\rm X}$, and EBWs in red, $k_{\rm ebw}$, are shown a) before, b) during, and c) after the density burst. Pink-shaded areas show evanescent regions.

agreement with the results of [58], where the evolution of the density profile is studied during ILMy crashes in a magnetic configuration with an inner 5/5 island chain.

Inhibition of PDI due to an increase in the edge density is also suggested by fluctuations in the emission of soft X-rays from the edge. Assuming bremsstrahlung as the dominant contribution, the total soft X-ray radiated power is proportional to $P_{\rm SXR} \propto Z_{\rm eff} n_{\rm e}^2 T_{\rm e}^{1/2}$, with $Z_{\rm eff}$ the effective charge [61]. Maxima in the emission along the outward XMCTS chords (corresponding to minima in the signal from inward chords) during PDI crashes (see figure 6.a-b) may, thus, suggest a density growth only outside the inversion surface, responsible for the suppression of the trapping mechanism. Accordingly, peaks in the emission of soft X-ray radiation along the outward chords also accompany bursts in the ABES density in the ABES-relevant discharge (see figure 6.d-e).

6. Conclusions

In this paper, we have shown an experimental correlation between low-threshold PDI and the trapping mechanism for UHWs within the non-monotonic density profile in the equatorial-plane magnetic island of W7-X. We have produced evidence of periodic crashes in PDI-related side-bands measured during X2-ECRH in the standard magnetic configuration when the microwave beams cross the O-point of the island. Correlation of crashes in the PDI signal with quasi-continuous oscillations in the plasma edge suggests excitation of PDI in the same region. We have additionally shown flattening of the density profiles within the island during fluctuations in the plasma edge in the standard configuration and have made use of the dispersion relations to study trapping of UHWs in experimental density profiles. The investigation has demonstrated suppression of the trapping mechanism when the edge density profile is flattened. This scenario is predicted to increase the PDI power threshold above the maximum gyrotron power and produce periodic crashes in the PDI-related side-bands. Such observations validate the hypothesis of PDI in the ECRH beams in the equatorial-plane magnetic island of W7-X, described in [35].

However, so far a discharge with high time resolution ABES density profiles and simultaneous PDI measurements is not available, allowing only an indirect comparison of the signals from different shots. A direct comparison (i.e. in a single discharge) between the evolution of the island density profile and the crashes in the PDI sidebands during ILMs that could conclusively validate the present results are planned for the next W7-X campaign, OP.2, starting at the end of 2022. During OP.2, a more systematic study of ILMs will be performed, the ABES will be operated more regularly, and the experience gained in the previous investiga-

tions of PDI will allow a straightforward identification of the most suitable scenarios for excitation of PDI.
PDI in the plasma edge may be responsible for anomalous deposition of the ECRH power away from the ECR, located in proximity of the magnetic axis. Since the power injected with a single gyrotron can currently reach hundreds of kW, the fraction of power drained by PDI from a pump microwave beam, even if small (e.g. 4 % theoretically predicted in [35]), could actually correspond to tens of kW. Moreover, excitation of electrostatic daughter waves in the edge may generate supra-thermal populations of ions and/or electrons and consequently overheat and degrade plasma facing probes, as observed in the previous W7-X campaign [42]. As recently reported in ASDEX Upgrade [39], daughter microwaves excited by PDI may not only corrupt the measurements of such systems, but also overload and permanently damage the diagnostic hardware. A deeper understanding of the mechanism of PDI in W7-X is, therefore, also relevant for assessing the need of proper shielding for microwave-based diagnostics.

Acknowledgements

A. Tancetti acknowledges the crucial theoretical contribution of E.Z. Gusakov and A.Yu. Popov to the present work.
This work has been supported by research grant 15483 from VILLUM FONDEN and the Enabling Research grant ENR-MFE19.DTU-03 from the EUROfusion Consortium. This work has been carried out within the framework of the EUROfusion Consortium, funded by the European Union via the Euratom Research and Training Programme (Grant Agreement No 101052200 — EUROfusion). Views and opinions expressed are however those of the author(s) only and do not necessarily reflect those of the European Union or the European Commission. Neither the European Union nor the European Commission can be held responsible for them.

Appendix A. Assessment of strong density fluctuations in ABES-relevant discharge

In order to identify density fluctuations in the plasma edge producing a flat ABES profile, two steps are followed. Initially, a moving average is computed for the signal in figure 6.d using a bin size $\delta t = 0.48\,\mathrm{ms}$, with bin mean, μ_i, and standard deviation, σ_i. Then, the mean, μ, and the standard deviation, σ, of the signal during the interval $t = 0.87 - 0.92\,\mathrm{s}$ are computed. The magenta solid and dashed lines in figure A1 show μ and $\mu + 2\sigma$, whereas orange circles and yellow error bars represent μ_i and σ_i for different bins. Gray-shaded regions in figure 6.d-f are plotted for events where $n_\mathrm{e} > \mu + 2\sigma$. The size of the shaded region is determined by the first and the last points around the peak where the bin mean drops below the mean, $\mu_\mathrm{i} < \mu$.

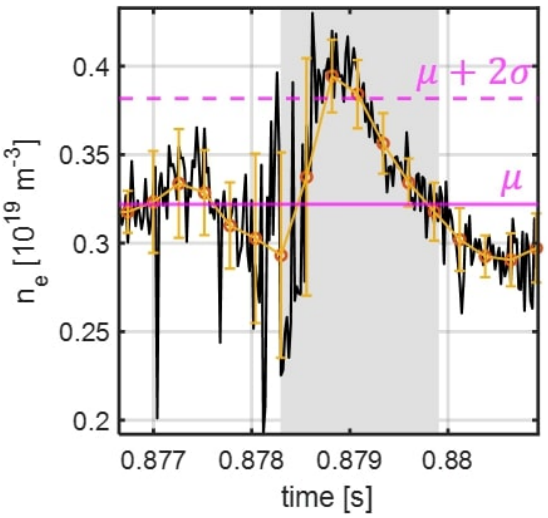

Figure A1: ABES density at $R \approx 6.233\,\mathrm{m}$ during one of the bursts in figure 6.d. The magenta solid and dashed lines show the mean μ and two standard deviations above the mean, $\mu + 2\sigma$, respectively, while orange circles and yellow error bars show the mean and standard deviation of the signal in different time bins. The gray-shaded region highlights the duration of the selected burst.

References

[1] H. Punzmann et al. *Physical Review Letters*, 103(6):064502, 2009.

[2] Q. Aubourg and N. Mordant. *Physical Review Letters*, 114(14):144501, 2015.

[3] F. Haudin et al. *Physical Review E*, 93(4):043110, 2016.

[4] M. Tokman et al. *Physical Review B*, 93(23):235422, 2016.

[5] D.J. Moss et al. *Nature Photonics*, 7(8):597–607, 2013.

[6] X. Guo et al. *Physical Review Letters*, 117(12):123902, 2016.

[7] T.J. Kippenberg and K.J. Vahala. *Science*, 321(5893):1172–1176, 2008.

[8] J.M. Dobrindt et al. *Physical Review Letters*, 101(26):263602, 2008.

[9] F. Brau et al. *Nature Physics*, 7(1):56–60, 2011.

[10] R.A. Stern and N. Tzoar. *Physical Review Letters*, 17(17):903, 1966.

[11] T.B. Leyser. *Space Science Reviews*, 98(3):223–328, 2001.

[12] A.V. Gurevich. *Physics-Uspekhi*, 50(11):1091, 2007.

[13] P.M. Bellan. *Fundamentals of Plasma Physics*. Cambridge university press, 2008.

[14] A.D. Piliya. In *Proc. 10th Int. Conf. Phenomena in Ionized Gases (Oxford)*, page 320. ed RN Franklin (Oxford: Donald Parsons & Co. Ltd.), 1971.

[15] F.W. Perkins and J. Flick. *The Physics of Fluids*, 14(9):2012–2018, 1971.

[16] M.N. Rosenbluth. *Physical Review Letters*, 29(9):565, 1972.

[17] A.D. Piliya. *Soviet Physics-JETP*, 37:629–632, 1973.

[18] E.Z. Gusakov and A.Yu. Popov. *Physical Review Letters*, 105(11):115003, 2010.

[19] E.Z. Gusakov and A.Y. Popov. *Nuclear Fusion*, 51(7):073028, 2011.

[20] A.Y. Popov and E.Z. Gusakov. *Journal of Experimental and Theoretical Physics*, 121(2):362–374, 2015.

[21] A.Y. Popov and E.Z. Gusakov. *EPL (Europhysics Letters)*, 116(4):45002, 2017.

[22] G.V. Lizunov et al. *Journal of Geophysical Research: Space Physics*, 106(A11):24755–24763, 2001.

[23] F. Li et al. *The Astrophysical Journal*, 924(1):33, 2022.

[24] A.V. Gurevich et al. *Physical Review Letters*, 75(13):2622, 1995.

[25] A.V. Gurevich et al. *Physics Letters A*, 231(1-2):97–108, 1997.

[26] P.A. Bernhardt et al. *Geophysical Research Letters*, 38(19), 2011.

[27] A. Samimi et al. In *Annales Geophysicae*, volume 30, pages 1587–1594. Copernicus GmbH, 2012.

[28] A.B. Altukhov et al. *EPL (Europhysics Letters)*, 126(1):15002, 2019.

[29] F.S. McDermott et al. *The Physics of Fluids*, 25(9):1488–1490, 1982.

[30] H.P. Laqua et al. *Physical Review Letters*, 78(18):3467, 1997.

[31] E. Westerhof et al. *Physical Review Letters*, 103(12):125001, 2009.

[32] S.K. Nielsen et al. *Plasma Physics and Controlled Fusion*, 55(11):115003, 2013.

[33] S.K. Nielsen et al. In *2016 41st International Conference on Infrared, Millimeter, and Terahertz Waves (IRMMW-THz)*, pages 1–2. IEEE, 2016.

[34] S.K. Hansen et al. *Nuclear Fusion*, 60(10):106008, 2020.

[35] A. Tancetti et al. *Nuclear Fusion*, 62(7):074003, 2022.

[36] G. Anda et al. *Fusion Engineering and Design*, 146:1814–1819, 2019.

[37] T. Stange et al. In *EPJ Web of Conferences*, volume 157, page 02008. EDP Sciences, 2017.

[38] N. Marushchenko et al. *Computer Physics Communications*, 185(1):165–176, 2014.

[39] S.K. Hansen et al. *Plasma Physics and Controlled Fusion*, 63(9):095002, 2021.

[40] D. Rapisarda et al. *Plasma Physics and Controlled Fusion*, 49(3):309, 2007.

[41] A.N. Karpushov et al. In *30th EPS Conference on Plasma Physics*, 2003.

[42] C. Killer et al. *Journal of Instrumentation*, 17(03):P03018, 2022.

[43] C. Killer et al. In *25th International Conference on Plasma Surface Interaction in Controlled Fusion Devices*. Korea Institute Fusion Energy, 2022.

[44] G.A. Wurden et al. In *45th EPS Conference on Plasma Physics*. European Physical Society, 2018.

[45] G.A. Wurden et al. In *46th EPS Conference on Plasma Physics*. European Physical Society, 2019.

[46] T. Andreeva et al. In *46th EPS Conference on Plasma Physics*. European Physical Society, 2019.

[47] J. Geiger et al. In *Proc. 28th IAEA Fusion Energy Conf.(FEC-2020, Virtual Event)*, 2021.

[48] M. Porkolab and B.I. Cohen. *Nuclear Fusion*, 28(2):239, 1988.

[49] A.G. Litvak et al. *Physics of Fluids B: Plasma Physics*, 5(12):4347–4359, 1993.

[50] E.Z. Gusakov and A.Yu. Popov. *Physics of Plasmas*, 23(8):082503, 2016.

[51] T.H. Stix. *Waves in Plasmas*. Springer Science & Business Media, 1992.

[52] H.L. Berk and D.L. Book. *The Physics of Fluids*, 12(3):649–661, 1969.

[53] C. Beidler et al. *Fusion Technology*, 17(1):148–168, 1990.

[54] T. Klinger et al. *Nuclear Fusion*, 59(11):112004, 2019.

[55] H.S. Bosch et al. *IEEE Transactions on Plasma Science*, 48(6):1369–1375, 2020.

[56] A. Dinklage et al. *Nature Physics*, 14(8):855–860, 2018.

[57] T.S. Pedersen et al. *Plasma Physics and Controlled Fusion*, 61(1):014035, 2018.

[58] R. Takacs et al. In *47th EPS Conference on Plasma Physics*. European Physical Society, 2021.

[59] D. Moseev et al. *Review of Scientific Instruments*, 90(1):013503, 2019.

[60] M. Stejner et al. *Review of Scientific Instruments*, 53(9):104003, 2014.

[61] C. Brandt et al. *Plasma Physics and Controlled Fusion*, 62(3):035010, 2020.

[62] M. Endler et al. *Fusion Engineering and Design*, 100:468–494, 2015.

[63] M. Hirsch et al. In *EPJ Web of Conferences*, volume 203, page 03007. EDP Sciences, 2019.

[64] L. Stephey et al. *Review of Scientific Instruments*, 87(11):11D606, 2016.

[65] N. Chaudhary et al. In *21st Joint Workshop on Electron Cyclotron Emission and Electron Cyclotron Resonance Heating. ITER Organization*, 2022.